IET Microwaves, Antennas & Propagation

Research Article

IET Journals
The Institution of Engineering and Technology

Optimisation of antenna arrays installed on non-conductive unmanned aerial vehicle

ISSN 1751-8725
Received on 27th March 2018
Revised 1st July 2018
Accepted on 30th July 2018
doi: 10.1049/iet-map.2018.5097
www.ietdl.org

Eduardo Yoshimoto[1], Edson Rodrigo Schlosser[1,2] ✉, Marcos Vinício Thomas Heckler[1]

[1]*Laboratory of Electromagnetics, Microwaves and Antennas – LEMA, Universidade Federal do Pampa (UNIPAMPA), Alegrete, RS, Brazil*
[2]*Center for Telecommunications Studies – CETUC, Pontifícia Universidade Católica do Rio de Janeiro (PUC-Rio), Rio de Janeiro, RJ, Brazil*
✉ *E-mail: edsonschlosser@unipampa.edu.br*

Abstract: This study presents the study of beamforming capabilities of arrays installed on a non-conductive unmanned aerial vehicle (UAV). The main purposes of this study are the application of a beamforming algorithm by including the airframe in the optimisations and the study of simplifications of the aircraft model, so as to allow performing full-wave simulations, even though the UAV is much larger than the operating wavelength. To validate the simplified electromagnetic model, antenna arrays have been designed and installed onto the UAV. Radiation pattern measurements demonstrate that the proposed simplifications yielded very good radiation pattern predictions and can be used as guidelines for simulation of other kinds of non-conductive aircrafts.

1 Introduction

The technical advances on communication systems have allowed the design of unmanned aerial vehicles (UAVs) for several applications, such as georeferencing of urban and rural areas, precision agriculture, search and rescue in disaster scenarios, border monitoring, traffic management or simply as a hobby. These UAVs can be controlled remotely or programmed to perform planned flights using global positioning system [1–3].

The flight range of some UAVs is limited by visual contact, which is not suitable for several applications. In order to overcome this limitation, a reliable communication link between the ground station and the UAV must be established, which is primarily dependent on the installed performance of the antennas.

Installed performance of antennas on aircraft is an important aspect on the aircraft design and has been studied since decades [4]. In [5], the influence of the airframe on the radiation pattern of various antenna models, such as monopoles, axial and circumferential slot antennas, is analysed. Recently, in [6], a four-port antenna installed on a small UAV (SUAV) has been studied. The SUAV was made of conducting material and operated as radiating element itself with different characteristic modes (CM). Such technique makes the aircraft to act as a dipole that can be polarised according to the phases impressed to each of the four feeding ports. Vogel *et al.* [7] also used the CM technique to analyse a small passenger jet aircraft. The resulting radiation pattern resembles that of a dipole antenna, which has the disadvantage of radiating nearly half of the power to the sky, hence being inefficient for air-ground communication.

Installed performance of patch antennas has been analysed in [8], where scaled models have been used to characterise the radiation properties of a 4×4 array for satellite navigation systems. The scaled aircraft models were covered with conductive paint. In [9], a linear antenna array is designed to operate at 1.27 GHz for circularly polarised synthetic aperture radar sensor mounted onto the bottom of an UAV.

In [10], an omnidirectional dual-polarised antenna to be installed on airplane is presented, but the influence of the airframe on the radiation pattern was not considered. The antenna was installed on the top of the fuselage, which may cause communication disruption in air-to-ground links during the flight, since there is normally a null in the radiation pattern below the aircraft.

Few contributions report on UAVs composed of dielectric materials. In [11], only a simplified model is considered, whilst the steering capability of an array installed on a functional UAV is studied in [12]. In this last paper, the antennas operate at 2.4 GHz and, at this frequency, the length of the airframe corresponds to $6.61\lambda_0$ and the wingspan to $9.14\lambda_0$, where λ_0 is the wavelength in free space. Hence, the UAV dimensions are not very large compared to the operation wavelength. The beam steering is achieved without optimisation of the sidelobes, since no amplitude tapering is considered.

This paper is dedicated to the accurate analysis and measurement of the performance of antenna arrays installed on a non-conductive UAV. In order to accelerate the analyses, simplifications of the electromagnetic model are proposed and validated by simulations. Another aspect is the consideration of pattern optimisation for different beamforming conditions by taking into account the influence of the airframe on the array performance. The optimisations are done by applying the particle swarm optimisation (PSO) technique for arrays operating at 5.8 GHz. Accurate results have been achieved by analysing the problem with full-wave techniques. Since the UAV exhibits wingspan of roughly $36\lambda_0$, where λ_0 is the wavelength in free space at 5.8 GHz, it is a model much larger in terms of electrical dimensions than the UAV analysed in [12]. Installed performance simulations of non-conductive UAVs with such large electrical dimensions are not trivial and can be assessed provided that special care is taken, as it will be addressed in the next sections. Moreover, the experimental characterisation of the designed array has been carried out with a complete and full-scale model, in contrast with [12], whereby only part of the UAV has been used for the radiation pattern measurements.

The paper is structured as follows. Section 2 presents analyses of the tridimensional aircraft model, whereby simplifications for the application of the finite-element method are proposed. Section 3 presents the antenna array theory, PSO formulation and radiation pattern synthesis for different proposals. Section 4 describes the design of the feeding system to provide the optimum amplitudes and phases for the array elements for the case of omnidirectional pattern in the yaw plane. The fabricated arrays have been mounted onto the UAV and far-field measurements have been carried out. Measured and simulation results are discussed finally in Section 5.

2 Simplified model for the non-conducting UAV

In order to perform optimisations, it is important to have an accurate model that is a trade-off between geometrical complexity and simulation accuracy. As suggested in [4], the electromagnetic

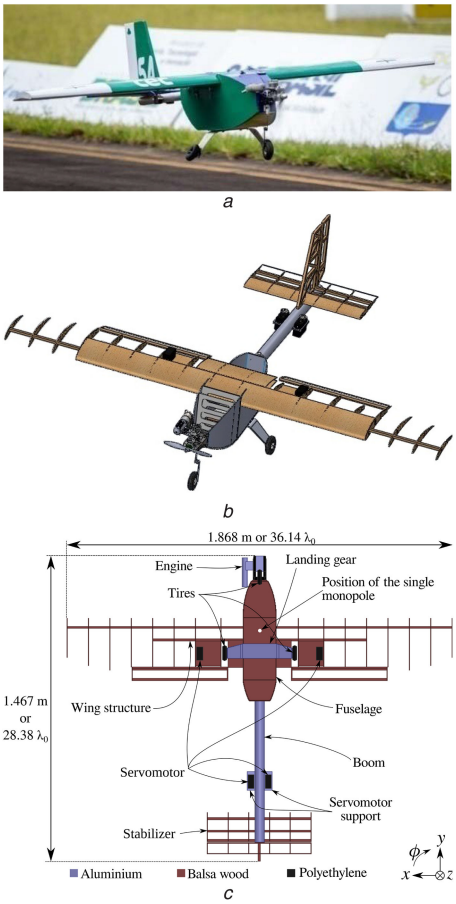

Fig. 1 *Dielectric UAV model*
(a) Photograph of the real UAV during the take-off, ***(b)*** Electromagnetic model in Ansys HFSS, ***(c)*** Original CAD model including components, materials and dimensions (height along the z-axis: 605 mm or $11.7\lambda_0$)

Table 1 Electromagnetic properties of the materials used to fabricate the UAV

	Relative permeability	Relative permittivity	Conductivity, S/m
wood	1	1	0
aluminium	1.000021	1	3.8×10^7
polyethelyne	1	2.25	0

model of the airframe should have only as many details as needed for the accurate determination of the radiation properties of the installed antennas.

The mechanical model was designed originally with a CAD software. For the electromagnetic simulations, the airframe has been imported into ansys HFSS electromagnetic simulator. A photograph of the UAV and its CAD model are shown in Figs. 1*a* and *b*, respectively. As it is usually the case, the UAV is composed of many parts and materials, such as wood, polyethylene and aluminium, as pointed out in Fig. 1*c*. The electromagnetic constitutive parameters of these materials are summarised in Table 1.

All the parts that compose the mechanical model are important for the fabrication of the UAV, but many of them do not influence strongly the installed performance of antennas. Therefore, a simplified model for the airframe can be obtained, so as to reduce the complexity and size of the mesh needed for the electromagnetic simulations. For instance, alleys, bolts, the thin plastic coating that covers part of the aircraft (such as wings and stabilisers), fixation hinges of movable surfaces (such as flaps, elevator and rudder) and many types of glue used in the construction can be removed. Additionally, the shape of some parts of the airplane was simplified. A summary of the modifications of the CAD model is

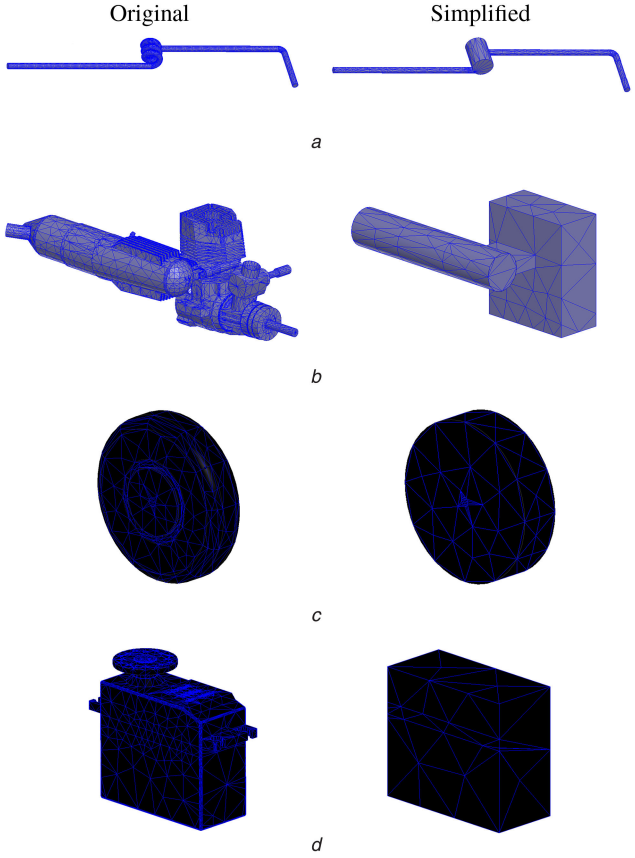

Fig. 2 *Original and simplified parts of the UAV*
(a) Front wheel support, ***(b)*** Engine, ***(c)*** Tires, ***(d)*** Servomotor

Table 2 Comparison of mesh sizes and simulation times for the original and the simplified model for the UAV

	Original model (tetrahedra)	Simplified model (tetrahedra)	Reduction, %
front wheel support	6313	2528	59.96
engine	56,217	447	99.20
servomotor	30,533	676	97.79
tires	12,322	1140	90.75
wing structure	16,702	4207	74.81
number of tetrahedra for the simplified parts	122,087	8998	92.63
number of tetrahedra for the complete airframes	377,444	264,355	29.96
simulation times	38 h 54 min 13 s	9 h 02 min 43 s	76.75

given in Fig. 2, where the original and the simplified parts of the aircraft are shown in detail.

In order to assess the impact of the geometrical simplifications in terms of computational time and overall mesh size, simulations have been carried out using the finite element boundary integral method available in the HFSS package. For this purpose, a single monopole has been placed in the position shown in Fig. 1*c*, which has been chosen due to the proximity of the antenna to some of the simplified parts (e.g. tires, engine and the tail wheel). The mesh sizes for both original and simplified models are summarised in Table 2, where the overall simulation times are also given. The number of mesh elements (tetrahedra) needed to model the original and simplified airframes are listed too.

With the geometrical simplifications, a reduction of roughly 30% in the total number of mesh elements (tetrahedra) has been

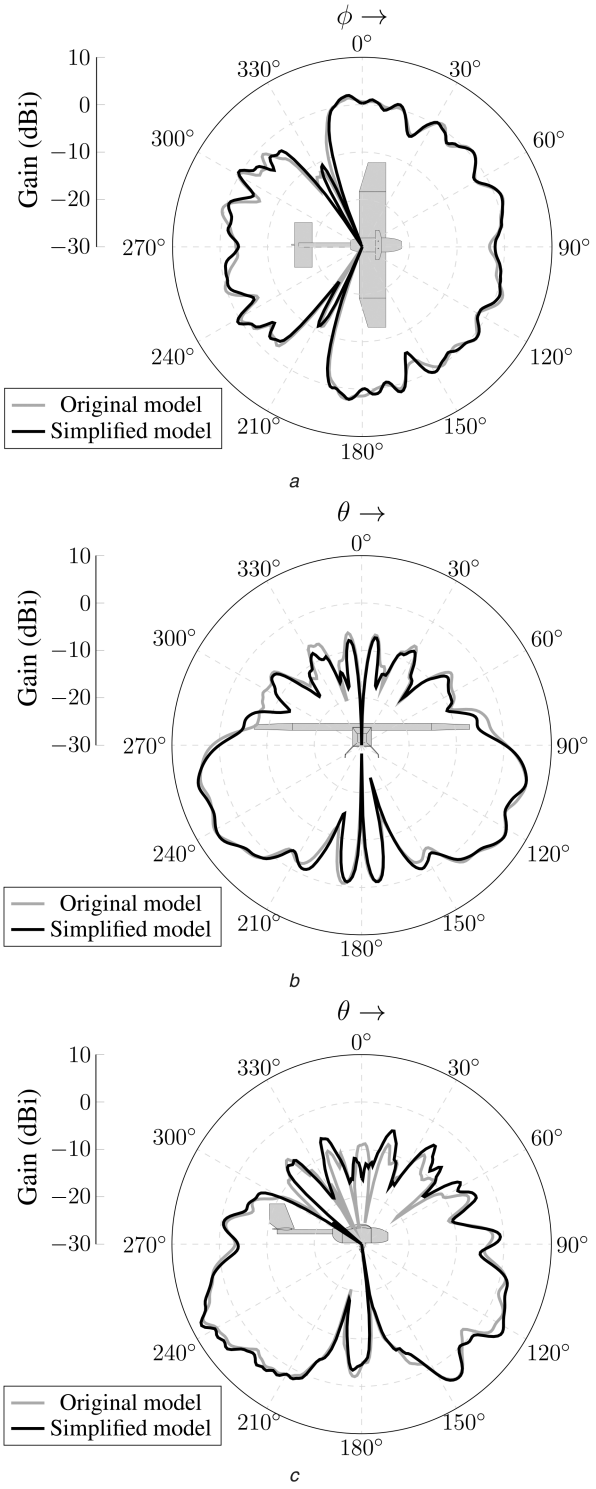

Fig. 3 *Radiation patterns for the original and the simplified UAV models*
(a) Yaw plane ($\theta = 90^{\circ}$), ***(b)*** Roll plane ($\phi = 0^{\circ}$), ***(c)*** Pitch plane ($\phi = 90^{\circ}$)

achieved, which resulted in a reduction in simulation time of 77%. The resulting radiation patterns are shown in Fig. 3, where it is evident that only very small deviations can be noticed between the patterns. Due to this result, the simplified aircraft model has been considered accurate enough for the analyses that follow.

3 Mathematical background for optimisation of antenna arrays installed on UAVs with PSO

Two antenna arrays have been designed and are depicted in Fig. 4*a*. Each array is composed of three monopoles, which are fed by microstrip lines, and is installed on the bottom surface of each wing. This position aims at avoiding the nulls present in the yaw plane pattern shown in Fig. 3*a*.

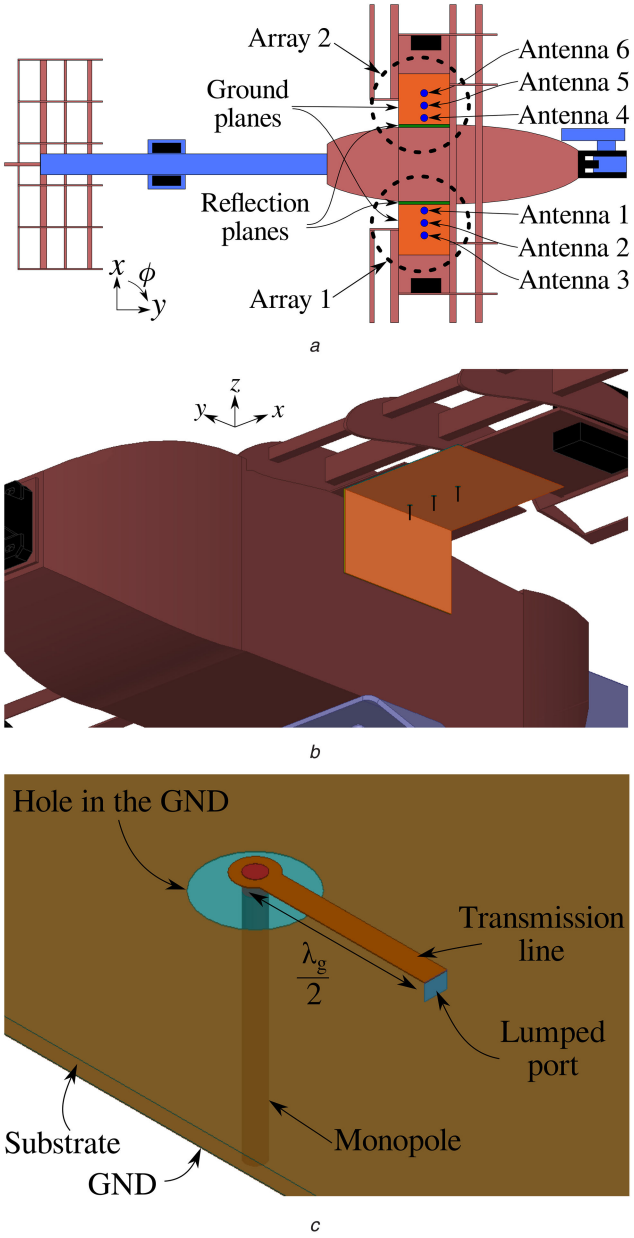

Fig. 4 *Antenna arrays installed onto the dielectric UAV*
(a) Schematic (bottom view), ***(b)*** Schematic, ***(c)*** Transition between a monopole and the microstrip line

3.1 Calculation of the radiation pattern in matrix notation

For the radiation pattern synthesis, a linear antenna array with elements placed along the x-direction will be considered. According to the classical array theory, the total electric field radiated by an antenna array composed of M elements is given by

$$\boldsymbol{E}_{\text{array}}(r,\theta,\phi) = \sum_{m=1}^{M} A_m \boldsymbol{E}_m(r,\theta,\phi) \mathrm{e}^{\mathrm{j}k_0 d(m-1)\sin\theta\cos\phi}, \quad (1)$$

where $\boldsymbol{E}_m$ is the electric field radiated by the mth array element, A_m is a complex beamforming coefficient attributed to the mth antenna, d is the uniform spacing between adjacent elements, k_0 is the propagation constant in free space and r is the radial distance from the origin of the coordinate system to an observation point in the far-field region. Equation (1) is the mathematical representation for the classical array theory, which is based on the assumption that the patterns of the individual elements are identical, whereby no mutual coupling takes place and the array is considered to exist in free space. However, by taking mutual coupling and the structure of the airplane into account, this assumption is not valid anymore.

In order to include these effects in the pattern synthesis, (1) has to be modified to

$$\boldsymbol{E}_{\text{array}}(r,\theta,\phi) = G\sum_{m=1}^{M} A_m\left[e_{m\theta}(\theta,\phi)\hat{\theta} + e_{m\phi}(\theta,\phi)\hat{\phi}\right], \tag{2}$$

where G is the Green's function of the free space, $e_{m\theta}$ and $e_{m\phi}$ represent the radiated electric field components of the mth antenna along θ and ϕ, respectively.

In the proposed approach, the term between the brackets must be calculated with a full-wave electromagnetic simulator. Since electromagnetic simulators calculate radiation patterns for discrete values of θ and ϕ, (2) must be transformed to a discrete form. For each direction (θ_g, ϕ_b) of the calculated pattern, (2) can be written as

$$\boldsymbol{E}_{\text{array}}(\theta_g,\phi_b) = \boldsymbol{A}\boldsymbol{e}(\theta_g,\phi_b), \tag{3}$$

where $\boldsymbol{E}_{\text{array}}$ and $\boldsymbol{A}$ are vectors with dimensions 1×2 and $1\times M$, respectively, whereby

$$\boldsymbol{A} = [a_1\angle\psi_1 \quad a_2\angle\psi_2 \ldots a_m\angle\psi_m \ldots a_M\angle\psi_M] \tag{4}$$

and $\boldsymbol{e}$ stands for an $M\times 2$ matrix defined as

$$\begin{aligned}\boldsymbol{e}(\theta_g,\phi_b) = [&\boldsymbol{e}_1(\theta_g,\phi_b) \quad \boldsymbol{e}_2(\theta_g,\phi_b)\ldots\\ &\ldots\boldsymbol{e}_m(\theta_g,\phi_b)\ldots\boldsymbol{e}_M(\theta_g,\phi_b)]^{\text{T}}\end{aligned} \tag{5}$$

with

$$\boldsymbol{e}_m(\theta_g,\phi_b) = [e_{m\theta}(\theta_g,\phi_b) \quad e_{m\phi}(\theta_g,\phi_b)], \tag{6}$$

where the symbol $[\,.\,]^{\text{T}}$ indicates the transpose of a vector and $1\leqslant m\leqslant M$. In (3), the radial dependency governed by G in (2) has been suppressed, since the synthesis is done considering the elemental patterns already in the far-field region. Therefore, the pattern shape does not vary with respect to r. In (4), a_ς and ψ_ς stand for the amplitude and phase of the beamforming coefficient of the ςth array element.

3.2 Mathematical background for the PSO implementation

The PSO is an evolutionary algorithm that profits from the principles of a swarm of bees [13, 14]. The bees fly around looking for flowers, hence their position changes over the time with varying speed. When a bee finds a place with high concentration of flowers, it calls the whole swarm to this location. The main three concepts involved in this process are: the movement of the bees, the memory of the locations with flowers found by each bee and the social interaction of the swarm, whereby the location of the highest concentration of flowers is informed to all the components of the swarm. The above behaviour can be converted into an optimisation problem by considering each bee as a particle and the best location as the optimum solution to the optimisation problem.

The optimisation algorithm must find the terms of the excitation vector $\boldsymbol{A}$ that synthesise the specified pattern. The PSO is started with the random generation of k particles to compose the initial swarm. Each particle contains all the variables that must be optimised (in this case, amplitudes and phases of the M beamforming coefficients). The method is based on the iterative update of each particle's position using the following representation for each variable:

$$\begin{aligned}\nu_n^k = w\nu_{n-1}^k &+ C_1\text{rand}(\,.\,)\left(p_{\text{best}}^k - p_{n-1}^k\right)\\ &+ C_2\text{rand}(\,.\,)\left(g_{\text{best}} - p_{n-1}^k\right),\end{aligned} \tag{7}$$

with

$$p_n^k = p_{n-1}^k + \nu_n^k, \tag{8}$$

where w is the inertia, C_1 and C_2 are coefficients associated with the particle's self-confidence and with the particle's trust in the swarm, respectively. The terms ν_{n-1}^k and ν_n^k are the last and the updated speed, p_{n-1}^k and p_n^k are the last and the updated position value of the kth particle, $rand(\,.\,)$ is a uniformly distributed random scalar value between 0 and 1, p_{best}^k is the best position found by the kth particle and g_{best} is the best position found by the swarm.

In the optimisation of an antenna array with PSO, a particle stands for a potential set of beamforming coefficients needed to synthesise the desired pattern. In matrix form, (7) and (8) can be rewritten as

$$\begin{aligned}\boldsymbol{V}_n^k = w\boldsymbol{V}_{n-1}^k &+ C_1\text{rand}(\,.\,)\left(\boldsymbol{P}_{\text{best}}^k - \boldsymbol{P}_{n-1}^k\right)\\ &+ C_2\text{rand}(\,.\,)\left(\boldsymbol{G}_{\text{best}} - \boldsymbol{P}_{n-1}^k\right),\end{aligned} \tag{9}$$

$$\boldsymbol{P}_n^k = \boldsymbol{P}_{n-1}^k + \boldsymbol{V}_n^k, \tag{10}$$

where $\boldsymbol{P}_n^k$ and $\boldsymbol{V}_n^k$ are vectors described, for this application, by

$$\begin{aligned}\boldsymbol{P}_{n-1}^k = [&a_1 \quad \psi_1 \quad a_2 \quad \psi_2 \ldots\\ &a_m \quad \psi_m \ldots a_M \quad \psi_M],\end{aligned} \tag{11}$$

$$\begin{aligned}\boldsymbol{V}_n^k = [&\Delta a_1 \quad \Delta\psi_1 \quad \Delta a_2 \quad \Delta\psi_2 \ldots\\ &\Delta a_m \quad \Delta\psi_m \ldots \Delta a_M \quad \Delta\psi_M],\end{aligned} \tag{12}$$

where $\boldsymbol{V}_{n-1}^k$ and $\boldsymbol{V}_n^k$ are the last and the updated speed vectors, and $\boldsymbol{P}_{n-1}^k$ and $\boldsymbol{V}_n^k$ are the last and the updated position vectors of the kth particle for M antennas. Each value corresponds to a dimension into the search space. After the last iteration, the variables of $\boldsymbol{G}_{\text{best}}$ correspond to the optimum values of the vector $\boldsymbol{A}$ as described in (4).

The particle's ability to serve as a solution to the optimisation problem must be evaluated by the particle's fitness, which is defined primarily as the deviation of the synthesised pattern $\boldsymbol{E}_{\text{array}}(\theta_g,\phi_b)$ from the specified mask $\boldsymbol{S}(\theta_g,\phi_b)$.

An additional issue must be taken into account during the optimisation of the excitation coefficients, since patterns to be synthesised have two particular parts: the first region defines the main beam, whereas the second one contains the sidelobes. In the former, the main beam generally should follow a desired contour, whereas simple level control is sought in the latter. Finally, the particle's fitness is calculated by

$$\text{fitness} = \sum_{j=1}^{2}\left[\frac{\xi_j}{N_j}\sum\left|\boldsymbol{S}(\theta_g,\phi_b) - \boldsymbol{E}_{\text{array}}(\theta_g,\phi_b)\right|\right], \tag{13}$$

where ξ_j denote the weight and N_j represent the total number of samples in the jth region, with $j=1$ for the main beam and $j=2$ for the region of the sidelobes.

The fitness as calculated by (13) takes into account only the radiation properties of the antenna under optimisation. However, in some applications, the minimisation of the effects of mutual coupling may also be a target. In this case, (13) must be modified accordingly so as to minimise impedance mismatch at the input of each array element.

4 Radiation pattern synthesis and feeder design

In order to compute the embedded patterns, the monopoles have been integrated into the simplified UAV model as detailed in Fig. 4*c*. Microstrip technology allows reducing size, weight, manufacturing costs and complexity of the feeder. The laminate Taconic RF-60A (dielectric constant $\varepsilon_r = 6.15$ and thickness of 0.79 mm) has been chosen for the design of the feeder, since it yields a thin and compact structure suitable for UAV applications.

During the optimisation of the radiation patterns in the yaw plane, the PSO has been set up with the parameters: $C_1 = C_2 = 0.5$,

Table 3 Optimised excitation coefficients and fitness function values for the case of beam switching (*m* is the element number according to Fig. 4*a*)

m	Excitation coefficients				
	$\phi_{\max}$ 0°	$\phi_{\max}$ 45°	$\phi_{\max}$ 90°	$\phi_{\max}$ 135°	$\phi_{\max}$ 180°
1	0.566∠172°	0.81∠181°	0.28∠0°	0	0
2	0.616∠0°	0.3∠70°	0.72∠321°	0	0
3	0.548∠165°	0.5∠0°	0.632∠281°	0	0
4	0	0	0.28∠0°	0.81∠181°	0.566∠172°
5	0	0	0.72∠321°	0.3∠70°	0.616∠0°
6	0	0	0.632∠281°	0.5∠0°	0.548∠165°
			Fitness Value		
	0.9734	2.186	3.4342	2.186	0.9734

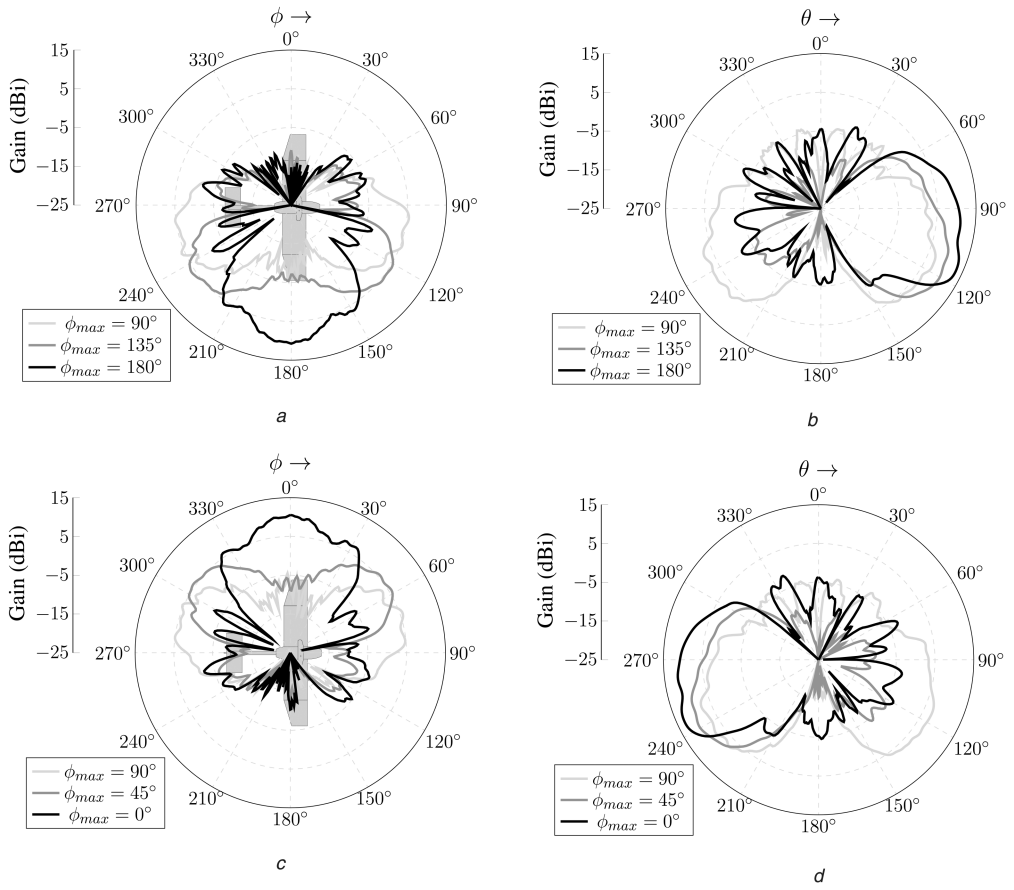

Fig. 5 *Optimised radiation patterns for the case of beam switching*
(a) Yaw plane for operation of array 1, ***(b)*** Elevation cuts in the direction of maximum radiation for array 1, ***(c)*** Yaw plane for operation of array 2, ***(d)*** Elevation cuts in the direction of maximum radiation for array 2

$w = 0.7$, $k = 50$ and $\xi_1 = 5\xi_2$. The search ranges for amplitudes and phases of the beamforming coefficients were 0 to 1 and 0° to 360°, respectively. The maximum number of iterations was set to 40.

4.1 Pattern synthesis for operation with switched beams

Considerable gain increase can be achieved with the two arrays by using beam switching. The whole yaw plane can be properly swept by steering the main beam to only six $\phi_{\max}$ directions: 90°, 135° and 180° with array 1, whilst keeping array 2 inactive, and 0°, 45° and 90° using the array 2 (with array 1 inactive). The optimum coefficients for these six pointing angles have been optimised with the PSO and are listed in Table 3. These beamforming coefficients have been introduced into the HFSS model and the resulting radiation patterns are presented in Fig. 5. Hangover between adjacent beams must occur as soon as the gain in the line-of-sight direction goes below 4 dBi, so as to avoid communication disruption.

4.2 Pattern synthesis for omnidirectional radiation

Another approach to achieve reliable communication between the UAV and the ground station is to consider an omnidirectional radiation pattern at each side of the UAV. In this case, the pattern to be synthesised for each array should follow a half-circumference contour in the angular range of $90^\circ \le \phi \le 270^\circ$ for array 1 and $-90^\circ \le \phi \le 90^\circ$ for array 2. Under these conditions, the resulting beamforming coefficients are listed in Table 4, which yielded a fitness value equal to 1.404. The beamforming coefficients have been introduced in HFSS and the resulting patterns are shown in Fig. 6.

By analysing Figs. 5*a*, 5*c* and 6*a*, larger gain can be achieved with beam switching with the expense of increasing the complexity of the feeder system, which must be adaptive so as to choose the correct pointing angle and the best set of excitation coefficients to be impressed at the array terminals. For this purpose, there is the need to use discrete components, such as PIN diodes [15, 16] or circuits composed of phase shifters and variable gain amplifiers

Table 4 Beamforming coefficients and resulting input impedances for omnidirectional radiation

m	Excitation coefficients	Z_{in}, Ω
1	$0.24\angle 0^{\circ}$	$6.9 - j1$
2	$1.00\angle 249^{\circ}$	$36.1 - j6.9$
3	$0.15\angle 161^{\circ}$	$102.5 - j53.9$
4	$0.24\angle 0^{\circ}$	$6.8 - j1.1$
5	$1.00\angle 249^{\circ}$	$36.2 - j6.9$
6	$0.15\angle 161^{\circ}$	$102.4 - j54$

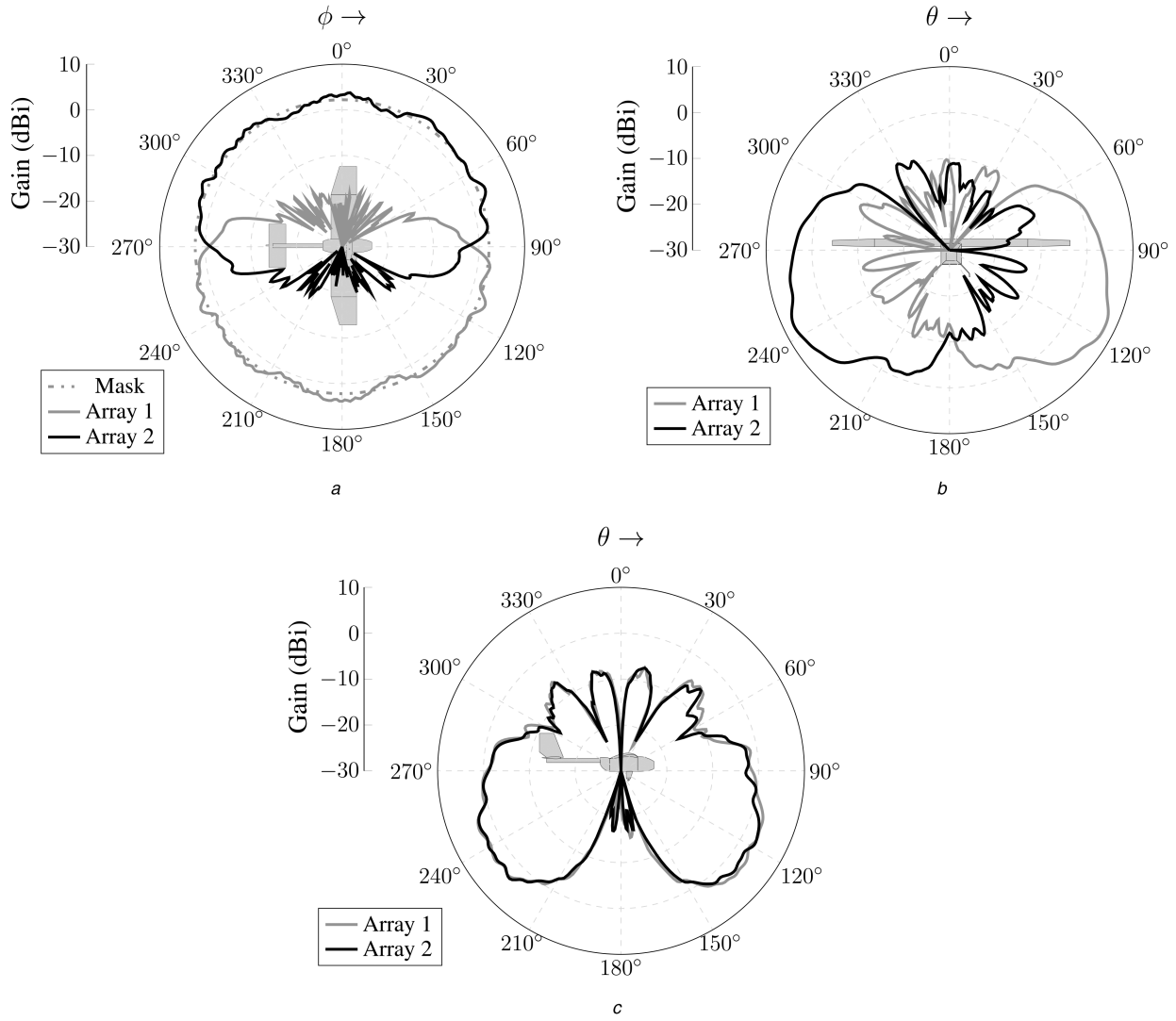

Fig. 6 *Optimised installed performance for omnidirectional radiation*
(a) Yaw plane, ***(b)*** Roll plane, ***(c)*** Pitch plane

controlled by a logic unit [17]. By making a trade-off between system complexity and performance, the case of omnidirectional pattern has been chosen for fabrication and validation of the proposed approach for the analysis of installed performance.

4.3 Feeder design

Using Ansys HFSS, the *Z*-parameters for the two arrays integrated onto the UAV CAD model have been computed and are equal to

$$\boldsymbol{Z} = \begin{bmatrix} \boldsymbol{Z}_{11} & \boldsymbol{Z}_{12} \\ \boldsymbol{Z}_{21} & \boldsymbol{Z}_{22} \end{bmatrix}, \tag{14}$$

where the elements $\boldsymbol{Z}_{ij}$ are 3×3 submatrices, where $\boldsymbol{Z}_{11}$, $\boldsymbol{Z}_{12}$, $\boldsymbol{Z}_{21}$ and $\boldsymbol{Z}_{22}$ are represented by (15)–(18), respectively. For $i = j$, the elements in the main diagonal of $\boldsymbol{Z}_{ij}$ stand for the self-impedances; the remaining elements of $\boldsymbol{Z}_{ij}$ are the mutual impedances existing between the monopoles inside each array. The submatrices $\boldsymbol{Z}_{ij}$ for $i \neq j$ quantify the mutual coupling between arrays 1 and 2

$$\boldsymbol{Z}_{11} = \begin{bmatrix} 28.1 - j2.5 & 2.2 - j15.9 & -1.7 + j7.8 \\ 2.2 - j15.9 & 28.4 - j10.9 & 1 - j14.6 \\ -1.7 + j7.8 & 1 - j14.6 & 28.3 - j10.9 \end{bmatrix} \Omega. \tag{15}$$

$$\boldsymbol{Z}_{12} = \begin{bmatrix} -0.01 + j0.02 & 0.1 - j0.1 & 0.01 - j0.03 \\ 0.1 - j0.1 & 0.1 - j0.04 & -0.1 - j0.1 \\ -0.04 - j0.02 & -0.1 - j0.1 & -0.04 + j0.3 \end{bmatrix} \Omega. \tag{16}$$

$$\boldsymbol{Z}_{21} = \begin{bmatrix} -0.04 - j0.02 & 0.1 - j0.1 & -0.01 + j0.02 \\ 0.1 - j0.1 & 0.1 - j0.04 & -0.1 - j0.1 \\ 0.01 - j0.03 & -0.1 - j0.1 & -0.04 + j0.3 \end{bmatrix} \Omega. \tag{17}$$

$$\mathbf{Z}_{22} = \begin{bmatrix} 28 - j2.6 & 2.2 - j16 & -1.6 + j7.6 \\ 2.2 - j16 & 28.2 - j11.1 & 0.8 - j14.6 \\ -1.6 + j7.6 & 0.8 - j14.6 & 28.2 - j11 \end{bmatrix} \Omega . \quad (18)$$

By inspecting (16) and (17), it comes out that $\mathbf{Z}_{12} \cong \mathbf{Z}_{21} \cong \mathbf{0}$; hence the coupling between the arrays can be neglected in the feeder design. The submatrices $\mathbf{Z}_{11}$ and $\mathbf{Z}_{22}$ are approximately the same due to the symmetry of the model. This allows the design of one feeder that is applicable for both arrays.

After importing the individual pattern of each monopole, the PSO has been run. The resulting excitation coefficients are listed in Table 4. The feeder has been designed based on the classical single-stub matching technique to transform the input impedances (Z_{in} values listed in Table 4) into completely real values: 33 Ω for antennas 2 and 5, and 50 Ω for the remaining monopoles. After this step, the power dividers were designed to deliver the desired power distribution to the antennas. The resulting impedance at the feeder input is well adapted to 50 Ω, so as to allow easy integration with standard RF components.

This design can still include some degree of flexibility for the antenna operation. The pattern can be switched to account for only one side of the UAV, if arrays 1 and 2 are supposed to work independently, or both arrays can be interconnected, hence resulting in the omnidirectional pattern in the yaw plane. For the latter case, the sketch shown in Fig. 7*a* can be used, whereby an 180° hybrid is used as a combiner. The resulting layout of the feeder designed for array 1 is detailed in Fig. 7*b*. For array 2, antennas 1, 2 and 3 in Fig. 7*b* should be replaced by antennas 4, 5 and 6, respectively. The prototype of the feeder for antenna 1 is shown in Fig. 7*c*. The measured reflection coefficient is shown in Fig. 7*d*, whereby the curve demonstrates that the impedance matching is very good in the operating band, indicated by the dotted lines, and the achieved bandwidth is much larger than required.

5 Validation of the installed performance

The fabricated array has been installed onto the UAV as shown in Fig. 8*a*. The radiation pattern measurement has been carried out according to the setup described in Figs. 8*b* and *c*. The comparison between computed and measured results for the yaw plane when only array 1 is active is presented in Fig. 9. Good agreement has been obtained, hence validating the proposed approach for the assessment of installed performance of antennas on dielectric UAVs.

6 Conclusion

The main purpose of this work was to propose an approach and to demonstrate its accuracy for the assessment of installed performance of antennas installed on dielectric UAVs with dimensions much larger than the wavelength. The installed performance can be improved by using an optimisation technique, which has been demonstrated by the implementation of the PSO. Accurate predictions can be achieved by using full-wave techniques, which could be applied after simplifications of the

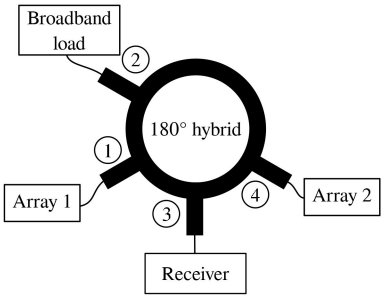

a

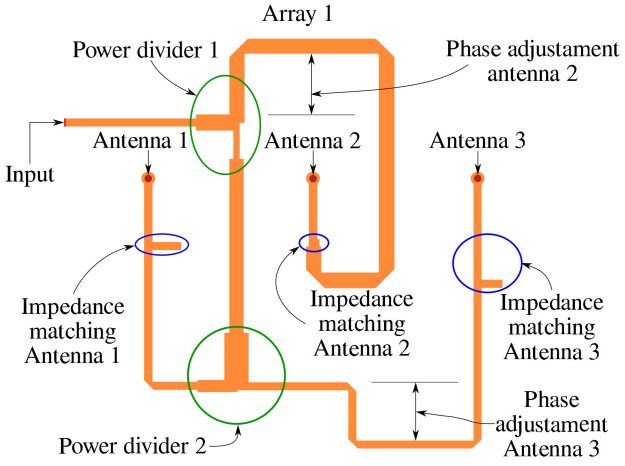

b

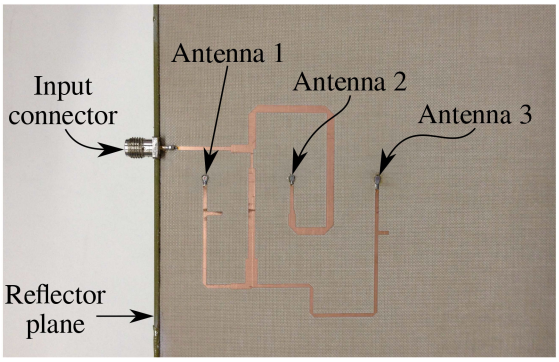

c

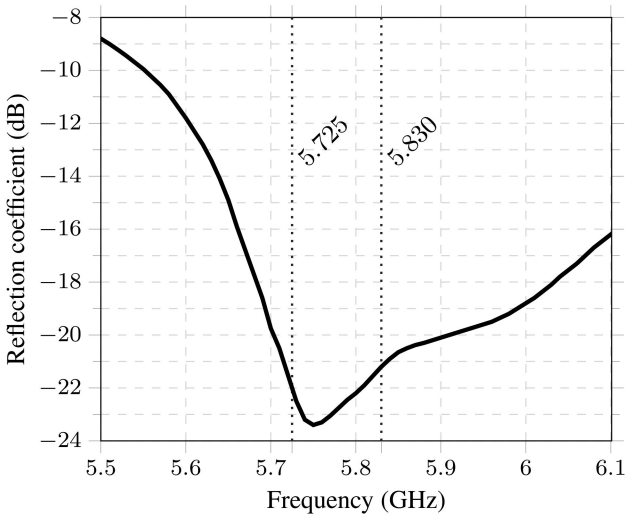

d

Fig. 7 *Feeder design in microstrip technology*

(a) Schematic interconnection between arrays 1 and 2, ***(b)*** Layout of the feeder for array 1, ***(c)*** Fabricated prototype, ***(d)*** Measured reflection coefficient

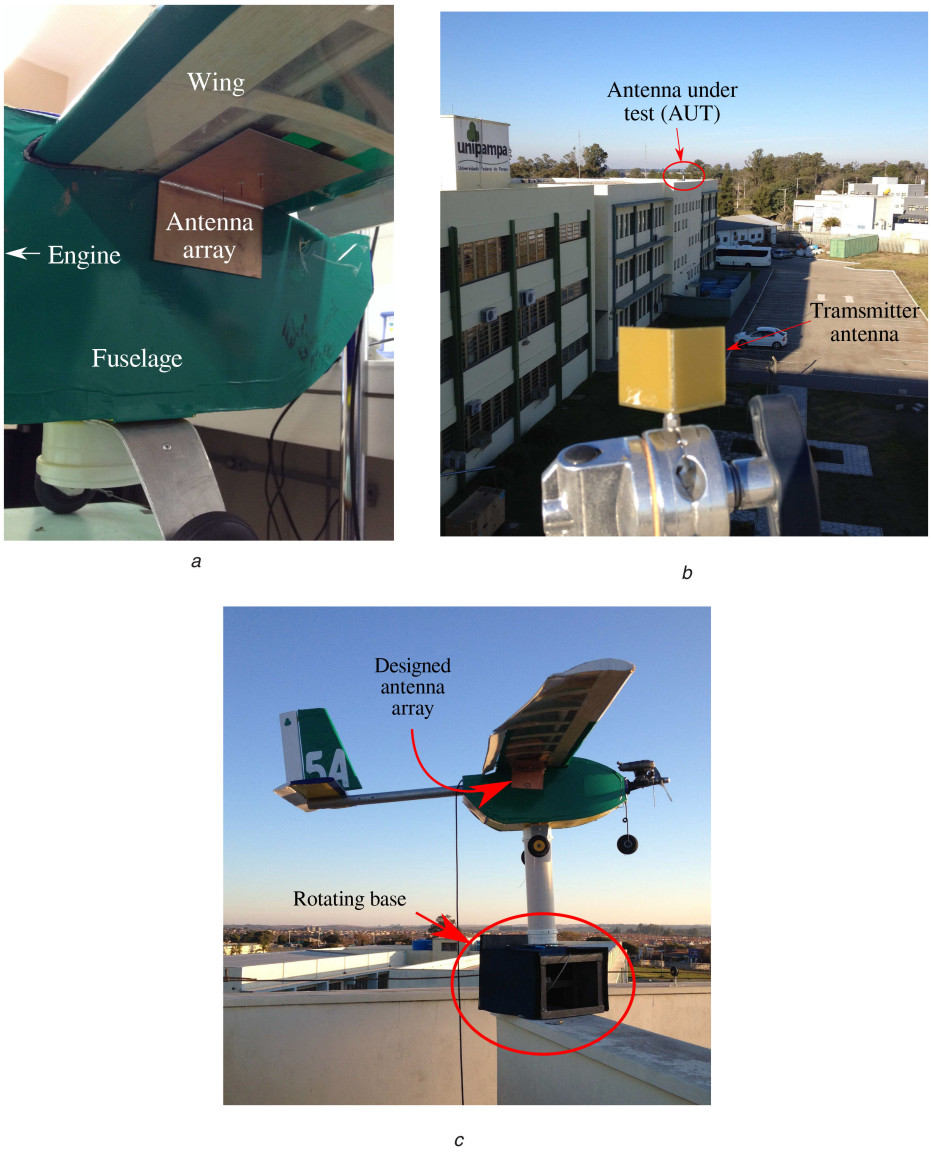

Fig. 8 *Measurement setup for experimental characterisation of the installed performance*
(a) Detail of the installation of array 1 onto the UAV, ***(b)*** Overview of the measurement setup, ***(c)*** UAV positioned for installed performance measurement in the yaw plane

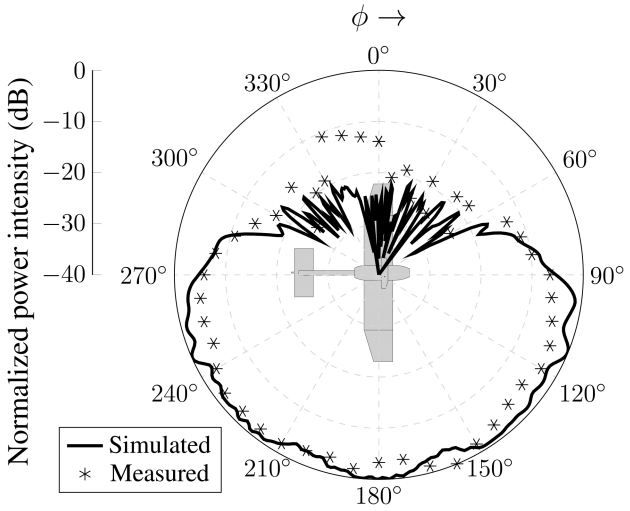

Fig. 9 *Comparison between simulated and measured radiation patterns in the yaw plane*

original UAV model were done, in order to reduce the computational effort.

The proposed approach has been demonstrated by designing and installing an antenna array onto a dielectric UAV. Radiation pattern measurements validate the numerical predictions of the proposed approach.

7 References

[1] Probst, L., Frideres, L., Pedersen, B., *et al.*: '*UAV systems for civilian applications*' (Business Innovation Observatory – European Commission, European Union, 2015, 58th edn.), pp. 1–15

[2] Whitehead, K., Hugenholtz, C.H., Myshak, S., *et al.*: 'Remote sensing of the environment with small unmanned aircraft systems (UASs), part 2: scientific and commercial applications', *Journal of Unmanned Vehicle Systems*, 2014, **2**, (3), pp. 86–102

[3] Samad, A.M., Kamarulzaman, N., Hamdani, M.A., *et al.*: 'The potential of unmanned aerial vehicle (UAV) for civilian and mapping application'. 3rd Int. Conf. System Engineering and Technology (ICSET), Shah Alam, Malaysia, August 2013, pp. 313–318

[4] Macnamara, T.: '*Introduction to antenna placement and installation*' (John Wiley & Sons, Hoboken, United States, 2010, 1st edn.)

[5] Burnside, W.D., Gilreath, M.C., Marhefka, R.J., *et al.*: 'A study of KC-135 aircraft antenna patterns', *IEEE Trans. Antennas Propag.*, 1975, **23**, (3), pp. 309–316

[6] Sow, S.-M., Guo, L., Zhou, S.-G., *et al.*: 'Electrically small structural antenna design for small UAV based on characteristics modes'. 11th European Conf. Antennas and Propagation (EUCAP), Paris, France, March 2017, pp. 2134–2138

[7] Vogel, M.H., Strydom, W.J., Jakobus, U., *et al.*: 'Aircraft antenna placement using characteristic modes'. 11th European Conf. Antennas and Propagation (EUCAP), Paris, France, March 2017, pp. 1758–1761

[8] Heckler, M.V.T., Dreher, A.: 'Performance of microstrip antenna arrays installed on aircraft'. *Aerosp. Sci. Technol.*, 2013, **26**, pp. 235–243

[9] Yohandri, A., Sumantyo, J.T.S.: 'Design of tilted beam circularly polarized antenna for CP-SAR sensor onboard UAV'. Proc. Int. Symp. Antennas and Propagation – ISAP, Okinawa, Japan, October 2016, pp. 658–659

[10] Liu, P., Li, Y., Zhang, Z., *et al.*: 'Omnidirectional dual-polarized antenna with sabre-like structure', *IEEE Trans. Antennas Propag.*, 2017, **65**, (6), pp. 3221–3225

[11] Sharawi, M.S., Ibrahim, M., Deif, S., *et al.*: 'A planar printed antenna array embedded in the wing structure of a UAV for communication link enhacement', *Prog. Electromagn. Res.*, 2013, **138**, pp. 697–715

[12] Sharawi, M.S., Aloi, D.N., Rawashdeh, O.A.: 'Design and implementation of embedded printed antenna arrays in small UAV wing structures', *IEEE Trans. Antennas Propag.*, 2010, **58**, (8), pp. 2531–2538

[13] Schlosser, E.R., Tolfo, S.M., Heckler, M.V.T.: 'Particle swarm optimization for antenna arrays synthesis'. Int. Microwave and Optoelectronics Conf. (IMOC), Porto de Galinhas, Brazil, November 2015, pp. 1–6

[14] Hu, J.-L., Chan, C.-H., Lin, S.-M.: 'Synthesis of shaped-beam pattern for mobile antenna'. Proc. IEEE Antennas and Propagation Society Int. Symp., Orlando, USA, July 1999, pp. 1596–1599

[15] de Luis, J.R., de Flaviis, F.: 'A reconfigurable dual frequency switched beam antenna array and phase shifter using PIN diodes'. Antennas and Propagation Society Int. Symp., Charleston, USA, June 2009, pp. 1–4

[16] Row, J.-S., Tsai, C.-W.: 'Pattern reconfigurable antenna array with circular polarization', *IEEE Trans. Antennas Propag.*, 2016, **64**, (4), pp. 1525–1530

[17] Magalhães, M.P., Engroff, A.M., Pereira, L.S., *et al.*: 'Synthesis of the radiation pattern of retrodirective antenna arrays using the particle swarm optimization algorithm'. Int. Microwave and Optoelectronics Conf. (IMOC), Porto de Galinhas, Brazil, November 2015, pp. 1–5